

Shape Reconstruction of Planar Flexible Spacecraft Structures using Distributed Sun Sensors

Thibaud Talon^{a,1}, Yulu Luke Chen^a, Sergio Pellegrino^{a,*}

^a*California Institute of Technology, Pasadena, CA, 91125, USA.*

Abstract

Flexible planar spacecraft, such as solar sails, phased antenna arrays and space solar power satellites vary their shape in flight and also may not have a known shape after deployment. To allow applications where spacecraft shapes are measured to allow the closed-loop correction of flight or payload parameters, this paper presents a method for measuring shapes with miniature sun sensors embedded within the structure. Two algorithms to reconstruct the shape of the structure from the two local angles to the sun are presented; the first one is geometry-based, whereas the second one uses a finite element model of the structure. Both algorithms are validated on a 1.3 m \times 0.25 m structure with 14 novel miniature sun sensors with an accuracy of 0.5°, developed for the present research. The structure was reconstructed to an accuracy better than one millimeter by both algorithms, after undergoing bending and torsional deformations. While the geometrically based algorithm is fast and accurate for small deformations, the finite element based algorithm performs better overall, especially for larger deformations.

Keywords: Surface reconstruction, Sun Sensor, Sensor Network

Nomenclature

*Corresponding author

Email addresses: `thibaud.talon@gmail.com` (Thibaud Talon), `luke2chen@gmail.com` (Yulu Luke Chen), `sergiop@caltech.edu` (Sergio Pellegrino)

¹Currently at OffWorld, Inc.

d	=	Sun sensor aperture width
\mathbf{d}_{fi}	=	Degrees of freedom of node i
e	=	Separation of sun sensor photodiodes
\mathbf{F}	=	Vector of external nodal loads
$\tilde{\mathbf{F}}$	=	Vector of non-zero load amplitudes
\mathbf{F}_d	=	Load redistribution matrix
h, H	=	Thicknesses of sun sensor
I_1, \dots, I_4	=	Light intensities on photodiodes of sun sensor
\mathbf{K}	=	Stiffness matrix
$\mathbf{n}(u, v)$	=	Normal to surface parameterized by $\mathbf{r}(u, v)$
N	=	Number of control points; number of external loads
$\mathbf{N}(u, v)$	=	Vector of shape functions evaluated at (u, v)
$\mathbf{r}(u, v)$	=	Position of the surface in the current configuration
$\mathbf{r}^0(u, v)$	=	Position of the surface in the reference configuration
$\frac{\partial \mathbf{r}}{\partial u}(u, v)$	=	First tangent vector to surface parameterized by $\mathbf{r}(u, v)$
$\frac{\partial \mathbf{r}}{\partial v}(u, v)$	=	Second tangent vector to surface parameterized by $\mathbf{r}(u, v)$
\mathbf{q}	=	Vector of unknowns of FESRA method
\mathbf{q}_{fi}	=	Displacement and rotation components of node i
\mathbf{R}	=	Rotation matrix
R_α, R_β	=	Normalized coordinates for sun sensor
t	=	Thickness of structure
\mathbf{t}	=	Translation vector
u, v	=	Curvilinear coordinates of surface
\hat{u}_i, \hat{v}_i	=	Coordinates of inextensibility grid in u -, v -direction for node i
u_S, v_S	=	Curvilinear coordinates of sensor S
w_i	=	Out-of-plane displacement of node i
x, y, z	=	Cartesian coordinates
α_S	=	Angle between sensor at location S and first tangent vector
β_S	=	Angle between sensor at location S and second tangent vector
$\phi_k(u, v)$	=	Basis function k

1. Introduction

Increasing interest in large lightweight space structures for applications such as solar sails, large antenna arrays and space solar power satellites has led to proposals of structural designs that are very flexible and subject to deformations that could impact their performance. For instance, the guidance of a solar sail is correlated with its shape as the thrust is produced from the reflection of sunlight onto the reflective structure. Similarly, a large antenna array requires co-phasing of the antennas as a non-planar shape would lead to phase errors.

Accurate shape measurement of these space structures can directly impact their performance and potentially enable new architectures or types of satellites, if on-board measurement systems can be incorporated within these structures without significant effect on the areal mass and operation of the spacecraft.

Commonly used shape measurement methods would require an imaging system to be placed in front of a surface. Sets of cameras or laser ranging devices generate a point cloud of the surface, from which the surface can be reconstructed [1, 2]. Simpler hardware, such as a single camera, is used in monocular surface reconstruction [3, 4, 5, 6, 7, 8, 9, 10]. Methods known as Shape-from-Template assume inextensibility of the deformation with feature-matching from an image, and Shape-from-Shading adds implicit measurements of the normals to the surface from the light reflected by the surface [8, 9, 10]. Such techniques require a minimum depth of view in front of the surface to measure. On a spacecraft, this could be done by either deploying a boom from the structure or building a second spacecraft that flies in formation. Shallow angle cameras have been used to measure the displacement of trackers on a surface [11, 12], achieving millimeter accuracy. Such methods are, however, susceptible to shading (physical blocking of the view of the camera due to the deformation), light condition restrictions and use relatively complex image processing software which limits their applicability.

This paper presents a different approach, which uses embedded angle sensors distributed over the surface to be reconstructed. The sensors measure the

local angles at specific locations of the structure, whose shape is then recovered by spatial integration. The angle measurements alone are not sufficient to reconstruct the shape of the surface because the distances between the sensors
35 need to be known or predicted to perform the spatial integration. Additional constraints are therefore implemented, similarly to vision-based methods such as monocular shape reconstruction algorithms. Two integration approaches are introduced in the paper. The first one is purely geometric and assumes inextensibility of the deformation from a known reference configuration (see figure
40 1). This approach has been used in vision-based research [3, 4, 5, 13, 14, 15]. The second algorithm replaces the inextensibility assumption with a mechanical model of the structure. The shape is then reconstructed with unknown boundary conditions that are solved for by matching the solved shape with the angle measurements.

45 The practical implementation of these algorithms requires sensors that can be readily embedded within a lightweight structure. Potential candidates include Inertial Measurement Units, or IMUs (a combination of an accelerometer with a magnetometer), which measure the angles from the gravity direction and Earth’s magnetic field. Several structural shapes have been reconstructed by
50 means of distributed IMUs [13, 14, 15, 16, 17]. Also, sun sensors, which measure the angle to the sun, have recently been investigated to reconstruct large surfaces in space [18, 19, 20]. Compared to IMUs, they have the advantage of being insensitive to acceleration or magnetic field disturbance. Boden and Hernando-Ayuso [18] considered the problem of reconstructing the shape of a
55 solar sail using the local sun angles measured with thin-film solar cells and the sail geometry was defined by a series of analytic functions. This approach is a precursor to the present work, but a single set of measurements was insufficient to determine the shape of the sail and hence a time series of measurements was required. Overall, the measurement accuracy was much lower than both
60 approaches presented in this paper.

A review of sun sensor designs is available in [21]. Most solutions consist of an array of photodiodes or light-sensing pixels coupled with an aperture mounted

on top [22, 23, 24, 25, 26, 27]. Their precision varies from a few degrees to less than an arc minute, but these existing designs are either bulky and expensive
65 or have low accuracy.

This gap in available technology has been addressed by the development of a novel miniature lightweight sun sensor design suited to applications that require many sensors to be placed on a flexible, ultralight structure. Also, both algorithms have been implemented and validated on an experimental testbed
70 that includes the new sensors, to assess the effects of any unmodeled physical effects and the limitations of the two algorithms.

The paper is arranged as follows. Section 2 presents the first algorithm that is used to reconstruct the shape of a surface, assuming the inextensibility of the deformation from an initially flat surface, and using the angle measurements from
75 a set of distributed sun sensors. This algorithm is called *Geometric Inextensible Shape Reconstruction Algorithm* (GISRA). Section 3 introduces the second algorithm, in which the inextensibility constraints are replaced with a finite element model of plate-like structures. In this model the shape is parametrized in terms of the applied boundary conditions whose unknown amplitudes are determined
80 by the angle measurements from the sun sensors. This algorithm is called *Finite Element Shape Reconstruction Algorithm* (FESRA). An experimental setup is introduced in section 4. The test structure consists of a 1.3 m \times 0.25 m thin aluminum plate fitted with 14 sun sensors. A novel sensor design, consisting of quad-photodiodes placed under a square aperture to create a simple pinhole
85 camera, was specifically developed for this experiment. The plate was deformed in bending and torsion and, to quantify the overall accuracy of the proposed reconstruction methods, the RMS error was calculated by comparing the reconstructed shape to independent, accurate measurements provided by an optical measurement system. The results of these experiments are presented in section
90 5. The RMS error is on the order of a millimeter and can be as low as 0.5 mm. It is shown that, while faster, GISRA can reconstruct nearly flat surfaces with good accuracy. FESRA, on the other hand, is able to reconstruct more heavily deformed surfaces. Section 6 concludes the paper.

2. Geometric Inextensible Shape Reconstruction Algorithm (GISRA)

95 The first algorithm used to reconstruct the shape of a surface from angle
 measurements is based on a set of equations that constrain the surface to match
 the measured angles at the sensor locations while imposing the inextensibility of
 the surface deformation from a given reference configuration. These equations
 are presented in the next subsection. Further details on the derivation of these
 100 equations can be found in chapter 2 of [28].

The practical implementation of this algorithm to real-world applications
 requires that the effects of the thickness of the structure, the offset of the sensors
 from the surface and the size of the sensors are accounted for. The required
 modifications of the equations are presented in the second subsection.

105 2.1. Surface Reconstruction

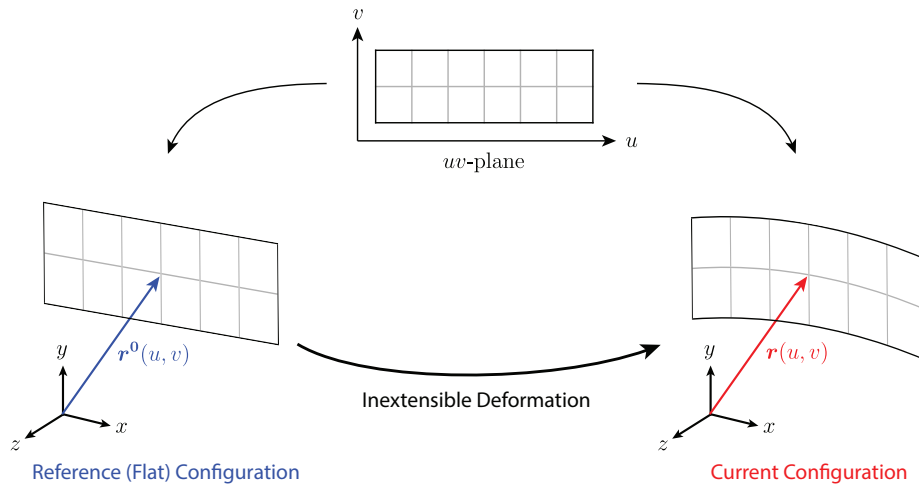


Figure 1: Definition of the problem. The 3D surface is a mapping of the 2D coordinates u, v to 3D. The reference configuration is known while the current configuration is unknown.

Shape Parametrization. A point on a surface is described by its two curvilinear coordinates u, v (see figure 1). The current 3D position of the point is

written as $\mathbf{r}(u, v)$ such that:

$$\mathbf{r} : X \subset \mathbb{R}^2 \longrightarrow \mathbb{R}^3$$

$$(u, v) \longmapsto \mathbf{r}(u, v) = \sum_{k=1}^N \mathbf{q}_k \phi_k(u, v) \quad (1)$$

where X is the curvilinear space, $\phi_k : X \rightarrow \mathbb{R}$ are basis functions, \mathbf{q}_k are unknown 3D points called control points, and N is the dimension of the function space.

The basis functions selected for the geometric reconstruction are 2D Lagrange polynomials weighted by the control points \mathbf{q}_k arranged in a 2D grid in the (u, v) -space (see grid in figure 2a). Different shape functions could be used, and Lagrange polynomials were selected for simplicity.

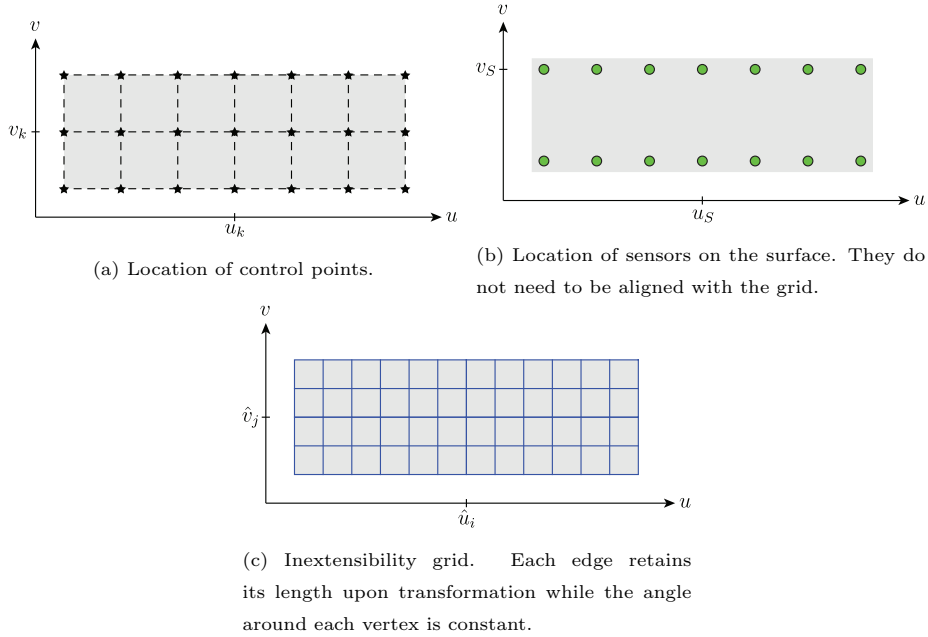


Figure 2: Parameters of the algorithm, defined in the uv -space.

The position of the control points is calculated by solving the following sensor equations and inextensibility constraints.

Sensor Equations. The sensors measure the angles between the local normals to the structure and light rays coming from a point source located at the origin

of the 3D coordinate system. For a sensor located on the surface at a location (u_S, v_S) (see figure 2b), the tangents of these angles can be calculated from:

$$\tan \alpha_S = \frac{\mathbf{r}(u_S, v_S) \cdot \frac{\partial \mathbf{r}}{\partial v}(u_S, v_S)}{\mathbf{r}(u_S, v_S) \cdot \mathbf{n}(u_S, v_S)} \frac{\|\mathbf{n}(u_S, v_S)\|}{\left\| \frac{\partial \mathbf{r}}{\partial v}(u_S, v_S) \right\|} \quad (2)$$

$$\tan \beta_S = -\frac{\mathbf{r}(u_S, v_S) \cdot \frac{\partial \mathbf{r}}{\partial u}(u_S, v_S)}{\mathbf{r}(u_S, v_S) \cdot \mathbf{n}(u_S, v_S)} \frac{\|\mathbf{n}(u_S, v_S)\|}{\left\| \frac{\partial \mathbf{r}}{\partial u}(u_S, v_S) \right\|} \quad (3)$$

115 where α, β are the angles between the normal and the u -direction and v -direction, respectively, $\mathbf{n}(u_S, v_S) = \frac{\partial \mathbf{r}}{\partial u}(u_S, v_S) \times \frac{\partial \mathbf{r}}{\partial v}(u_S, v_S)$ is the normal to the surface at the sensor location, and $\mathbf{r}(u_S, v_S)$ coincides with the direction of the light ray, since the light source is located at the origin of the coordinate system.

120 **Inextensibility Constraints.** Inextensibility conditions are derived from a discretization of the metric tensor, which is used in differential geometry to measure the length of segments on curved surfaces [29, 30]. By imposing the condition that the metric tensor does not change, the length of any segment drawn on the surface stays the same. The (flat) shape of the surface before the
125 transformation is called reference configuration, as shown in figure 1.

A discretization of the metric tensor is performed by defining a regular grid on the surface (see figure 2c). The coordinates of the grid are \hat{u}_i and \hat{v}_j . Each edge of the grid is constrained to have the same length in the current and reference configurations. To keep the angles at each node of the grid invariant, the dot product of the tangent vectors to the surface has to remain constant. Hence, the following constraint equations are written:

$$\int_{\hat{u}_i}^{\hat{u}_{i+1}} \left\| \frac{\partial \mathbf{r}}{\partial u}(u, \hat{v}_j) \right\| du = \int_{\hat{u}_i}^{\hat{u}_{i+1}} \left\| \frac{\partial \mathbf{r}^0}{\partial u}(u, \hat{v}_j) \right\| du \quad (4)$$

$$\int_{\hat{v}_j}^{\hat{v}_{j+1}} \left\| \frac{\partial \mathbf{r}}{\partial v}(\hat{u}_i, v) \right\| dv = \int_{\hat{v}_j}^{\hat{v}_{j+1}} \left\| \frac{\partial \mathbf{r}^0}{\partial v}(\hat{u}_i, v) \right\| dv \quad (5)$$

$$\frac{\partial \mathbf{r}^T}{\partial u}(\hat{u}_i, \hat{v}_j) \frac{\partial \mathbf{r}}{\partial v}(\hat{u}_i, \hat{v}_j) = \frac{\partial \mathbf{r}^{0T}}{\partial u}(\hat{u}_i, \hat{v}_j) \frac{\partial \mathbf{r}^0}{\partial v}(\hat{u}_i, \hat{v}_j) \quad (6)$$

where \mathbf{r}^0 is the reference configuration.

Solution Method. By gathering the sensor equations 2 and 3 at each sensor location with the inextensibility equations 4, 5 for each edge and equation 6 for
130 each node of the inextensibility grid, a system of equations with $3N$ unknowns (the three coordinates of the control points) can be written. By including a sufficiently large number of sun sensors, it is ensured that this system of equations is overconstrained and in this case the system can be solved using the Levenberg-Maquard algorithm. It is shown in [28] that the solution converges if
135 the number of angle measurements (which is twice the number of sun sensors) is greater than N and the total number of equations greater than $3N$.

Well-Posedness. A study of the singularities of the sensor equations and inextensibility constraints [28] has shown that the singularities of the two sets
140 of equations are mutually exclusive except for 3 rigid rotations around the origin, which can be eliminated by constraining the motion of some control points. A fourth singularity is associated with the distance between the surface and the origin, i.e. the location of the light source. When this distance is large, a translation of the surface away from the light source has a small impact on the measured angles. If the light source is considered a “point at infinity” which is
145 a valid assumption for the sun, then this translation can be removed by fixing a control point. Otherwise, this singularity can lead to convergence issues in the solution, which can be eliminated by determining the position of a control point or by measuring the distance between the surface and the light source, with a
150 different type of sensor.

2.2. Practical Implementation

The previous equations need to be modified to account for the thickness of the surface, the offset of the sensors from the surface and the sensor size. A mathematical treatment of these effects is provided next whereas more practical
155 aspects are considered in section 4.

The surface previously defined by $\mathbf{r}(u, v)$, where both the control points and the inextensibility grid are located, corresponds to the mid-surface of the structure, which remains inextensional due to the inextensibility constraints presented in section 2.1. However, it should be noted that actually the front of the structure is of interest, rather than the mid-surface, and therefore an offset of half the thickness along the local normal has to be applied during post-processing. Assuming that the normals to the underformed mid-surface are also normal to the deformed surface (this is known as the Kirchhoff hypothesis for thin shells [31]):

$$\mathbf{s}(u, v) = \mathbf{r}(u, v) + \frac{t}{2} \frac{\mathbf{n}(u, v)}{\|\mathbf{n}(u, v)\|} \quad (7)$$

where $\mathbf{s}(u, v)$ is the front surface, t is the thickness of the structure, and $\mathbf{n}(u, v)$ is the local normal.

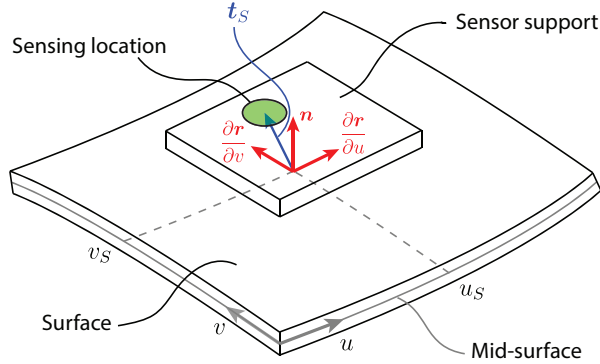


Figure 3: Offset of sensor from the mid-surface of the structure. The fixed offset \mathbf{t}_S is defined in the local reference system (in red).

The equations that need to be modified are those related to the angle measurements (equations 2 and 3), because the sensors are not located on the mid-surface, but are offset by a fixed distance as shown in figure 3. Furthermore, they can be assumed to be rigid and therefore the local tangent and normal vectors in the equations are calculated in the middle of the rigid support of the sensors, which approximates the actual direction of the sensor. The sensing element is offset, in this local reference system, by a fixed vector \mathbf{t}_S (see figure

3). Therefore, the angle equations become:

$$\tan \alpha_S = \frac{\mathbf{d}_S \cdot \frac{\partial \mathbf{r}}{\partial v}(u_S, v_S) \|\mathbf{n}(u_S, v_S)\|}{\mathbf{d}_S \cdot \mathbf{n}(u_S, v_S) \left\| \frac{\partial \mathbf{r}}{\partial v}(u_S, v_S) \right\|} \quad (8)$$

$$\tan \beta_S = -\frac{\mathbf{d}_S \cdot \frac{\partial \mathbf{r}}{\partial u}(u_S, v_S) \|\mathbf{n}(u_S, v_S)\|}{\mathbf{d}_S \cdot \mathbf{n}(u_S, v_S) \left\| \frac{\partial \mathbf{r}}{\partial u}(u_S, v_S) \right\|} \quad (9)$$

where \mathbf{d}_S is the vector between the center of the 3D reference system (with the light source at the origin) and the center of the light sensor, offset by \mathbf{t}_S in the local reference system. This vector can be written as:

$$\mathbf{d}_S = \mathbf{r}(u_S, v_S) + \mathbf{R}_S \mathbf{t}_S \quad (10)$$

where \mathbf{R}_S is the local rotation matrix at the sensor location which is defined as the concatenation of the tangent and normal unit vectors:

$$\mathbf{R}_S = \begin{bmatrix} \frac{\frac{\partial \mathbf{r}}{\partial u}(u_S, v_S)}{\left\| \frac{\partial \mathbf{r}}{\partial u}(u_S, v_S) \right\|} & \frac{\frac{\partial \mathbf{r}}{\partial v}(u_S, v_S)}{\left\| \frac{\partial \mathbf{r}}{\partial v}(u_S, v_S) \right\|} & \frac{\mathbf{n}(u_S, v_S)}{\|\mathbf{n}(u_S, v_S)\|} \end{bmatrix} \quad (11)$$

3. Finite Element Shape Reconstruction Algorithm (FESRA)

This section introduces an alternative shape reconstruction where the in-
 160 extensibility conditions of the GISRA algorithm, presented in section 2, are
 replaced with the stiffness equations generated from a finite element model of
 the structure. The parametrization of the deformation of the surface is also
 generated from this finite element formulation, following an approach similar to
 section 2.

165 The present study is limited to small deformations of plate-like structures,
 such as the structure used in the experiment shown in section 4. A static, linear-
 elastic model based on plate finite elements is used to capture the behavior of
 the structure.

Shape Parametrization. The undeformed surface, defined locally in the
 170 (x, y, z) reference frame (see figure 4), coincides with the x, y plane. The de-
 formed surface is defined by the degrees of freedom of the nodes of the finite
 element mesh, consisting of triangular elements. The shape functions defined
 locally for each element interpolate between the nodal degrees of freedom.

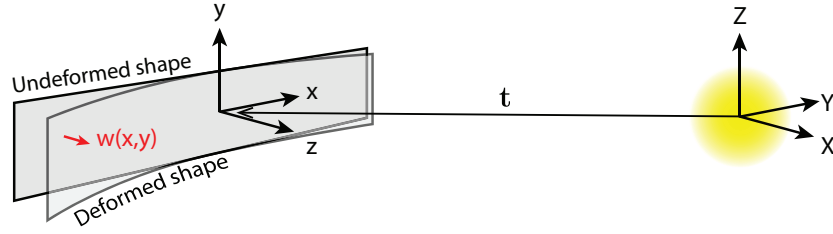


Figure 4: Definition of reference frames for the problem. The reference configuration has the light source at the origin and the current reference is used to define the finite element model of the structure.

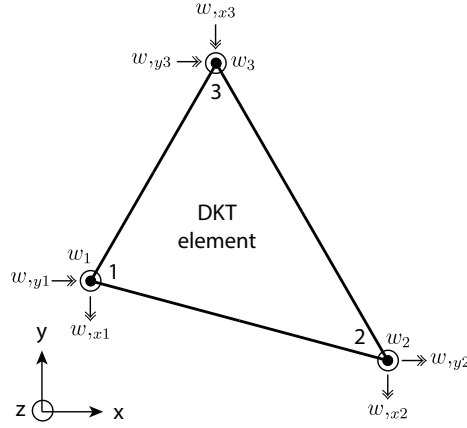


Figure 5: Definition of the degrees of freedom used in the formulation of the DKT element.

A plate bending model that neglects the transverse shear deformation of the structure is considered (Kirchhoff plate theory). Hence, the degrees of freedom of node i are the out-of-plane displacements and the rotation components around the x - and y -axes:

$$\mathbf{q}_{fi} = \begin{bmatrix} w_i \\ w_{,xi} \\ w_{,yi} \end{bmatrix} \quad (12)$$

where w is the out-of-plane deflection, and $w_{,x} = \frac{\partial w}{\partial x}$, and $w_{,y} = \frac{\partial w}{\partial y}$ the first derivatives (slopes). These degrees of freedom are shown in figure 5; note that the positive rotation components are defined by the positive slopes.

The reconstructed surface is translated to a reference frame with the light

source at its origin, in order to use equations 8 and 9 (see figure 4). The position of a point on the surface in the (X, Y, Z) reference frame is:

$$\mathbf{r}(x, y) = \mathbf{t} + \begin{bmatrix} x \\ y \\ 0 \end{bmatrix} + \begin{bmatrix} \mathbf{0} \\ \mathbf{0} \\ \mathbf{N}(x, y) \end{bmatrix} \mathbf{q}_f \quad (13)$$

where \mathbf{t} is a translation vector, $\mathbf{N}(x, y)$ is the row vector of the shape functions evaluated at (x, y) and \mathbf{q}_f is the vector of all degrees of freedom of the model. Note that, since the problem is invariant for any rotation around the light source,
180 no rotation is necessary.

The kinematic boundary conditions are chosen such as to ensure small deformations in the (x, y, z) reference frame. This approach avoids rigid-body motions in the formulation. An example of a suitable boundary condition is clamping a node (i.e., setting all of its degrees of freedom equal to 0). Another
185 example is setting equal to zero the out-of-plane deflection of three non-aligned nodes.

Finite Element Model. A linear, static state equation links the (small) displacement components for all Degrees of Freedom (DoF) to the corresponding external loads:

$$\mathbf{K}\mathbf{q}_f = \mathbf{F} \quad (14)$$

where \mathbf{K} is the stiffness matrix of the finite element model, \mathbf{q}_f is the vector of degrees of freedom, and \mathbf{F} is the vector of external nodal loads (interpolation of
190 the external loads to the nodal DoF). The total number of degrees of freedom in the model is three times the number of nodes, see equation 12.

Different models can be used to derive the stiffness matrix \mathbf{K} . The Discrete Kirchoff Triangular (DKT) element [31] is considered among the best Kirchoff plate elements [31, 32] and was chosen for the present study. The degrees of
195 freedom for this element are defined in figure 5.

The shape functions for the DKT element are complete quadratic polynomials, and their expressions can be found in section 7.1 of [31].

For the current problem, only concentrated loads are applied as boundary conditions, without any kinematic boundary conditions other than those described above, to remove rigid motions. The location of these concentrated loads is known, but their amplitude is not known and hence it is left as an unknown and it is determined by the angle measurements of the sensors. It should be noted that these unknown concentrated loads are, in effect, the reactions applied to the structure by kinematic constraints acting on it. The actual loads applied to the structure, which are mostly distributed, are known and are directly accounted for in the solution.

Let N be the total number of external loads (forces and moments). The force vector \mathbf{F} can be re-written as:

$$\mathbf{F} = \mathbf{F}_d \tilde{\mathbf{F}} \quad (15)$$

where $\tilde{\mathbf{F}}$ is a vector of dimension N concatenating the amplitudes of the external concentrated loads and \mathbf{F}_d is a conversion matrix, with the number of rows equal to the total number of DoF and the number of columns equal to N , that redistributes the concentrated loads to their nodal values. The matrix \mathbf{F}_d is mostly filled with zeros. It has ones to transform each concentrated load into a set of nodal forces and moments.

Unknowns. Considering equations 13, 14, and 15, the unknowns of the algorithm are:

1. the degrees of freedom of the nodes
2. the amplitudes of the concentrated loads
3. the translation of the surface

and they can be written as:

$$\mathbf{q} = \begin{bmatrix} \mathbf{q}_f \\ \tilde{\mathbf{F}} \\ \mathbf{t} \end{bmatrix} \quad (16)$$

The dimension of this vector can be large for dense meshes but it is determined
 220 by an equally large number of equations.

Constraint and Sensor Equations. The finite element model in equation 14 replaces the inextensibility equations defined in section 2 (equations 4, 5, and 6). The equations for the algorithm are therefore:

1. the state equation from the finite element model, equation 14:

$$\mathbf{K}\mathbf{q}_f = \mathbf{F}_d\tilde{\mathbf{F}} \quad (17)$$

2. the sensor equations, equations 8, 9, which can be re-written as:

$$\tan \alpha_S = \frac{\mathbf{d}_S \cdot \frac{\partial \mathbf{r}}{\partial y}(x_S, y_S)}{\mathbf{d}_S \cdot \mathbf{n}(x_S, y_S)} \frac{\|\mathbf{n}(x_S, y_S)\|}{\left\| \frac{\partial \mathbf{r}}{\partial y}(x_S, y_S) \right\|} \quad (18)$$

$$\tan \beta_S = -\frac{\mathbf{d}_S \cdot \frac{\partial \mathbf{r}}{\partial x}(x_S, y_S)}{\mathbf{d}_S \cdot \mathbf{n}(x_S, y_S)} \frac{\|\mathbf{n}(x_S, y_S)\|}{\left\| \frac{\partial \mathbf{r}}{\partial x}(x_S, y_S) \right\|} \quad (19)$$

225 where \mathbf{d}_S is defined in equation 10 with $\mathbf{r}(u_S, v_S)$ obtained from equation 13.

Note that if the sensors are attached to the nodes of the finite element model, the local tangent and normal vectors have the expressions:

$$\frac{\partial \mathbf{r}}{\partial x}(x_S, y_S) = \begin{bmatrix} 1 \\ 0 \\ w_{,xS} \end{bmatrix} \quad \frac{\partial \mathbf{r}}{\partial y}(x_S, y_S) = \begin{bmatrix} 0 \\ 1 \\ w_{,yS} \end{bmatrix} \quad \mathbf{n}(x_S, y_S) = \begin{bmatrix} -w_{,xS} \\ -w_{,yS} \\ 1 \end{bmatrix} \quad (20)$$

which are all unit vectors, to the first order.

Because equation 17 generates a number of equations equal to the number of degrees of freedom of the finite element model, the number of sensor equations
 230 (which is twice the number of sun sensors) needs to be equal to or greater than the number of unknown nodal loads N plus 3, which is the size of the translation vector.

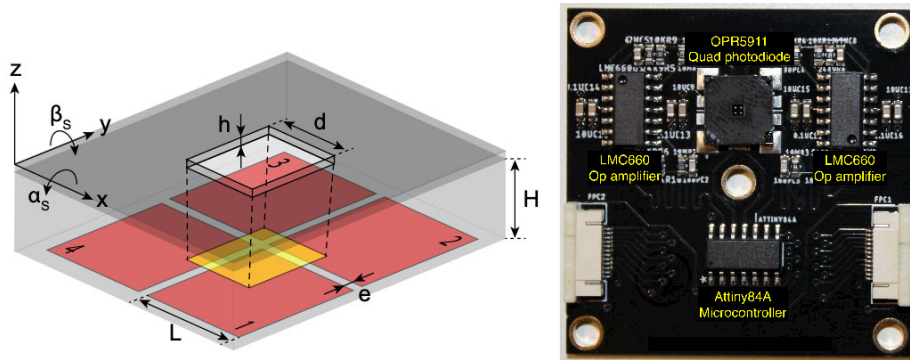
Solution Method. The equations 17, 18, and 19 define a system of equations
 235 whose unknown is the vector \mathbf{q} (equation 16). This system has been solved
 using the Levenberg-Marquardt algorithm. In practice, the MATLAB function
 fsolve was used with default tolerance parameters.

4. Experimental Setup

This section presents the hardware for the experiments and the numerical
 240 parameters for the shape reconstruction.

4.1. Sun Sensors

A schematic of the sun sensor designed and built for this research is shown in
 figure 6a. The geometric parameters of the sensors are defined in the figure. The
 sensor consists of a quad-photodiode that measures the light intensity generated
 245 by a light spot created by a square aperture located above the photosensitive
 plane. As the sensor rotates around x and y , with respect to a fixed point light
 source, the spot moves over the quad-photodiode which consequently varies the
 intensity reading of each photodiode.



(a) Schematic of sun sensor made from a quad-photodiode (red) and a square aperture. (b) 4×4 cm board including the sensor and its electronics.

Figure 6: Details of the sun sensor.

The coordinates of the centroid of the light spot can be calculated from the
 intensities of the four photodiodes (named I_1 through I_4). Let R_β (respectively

R_α) be the normalized coordinates in the x-direction (respectively. y-direction):

$$R_\alpha = \frac{(I_1 + I_4) - (I_2 + I_3)}{I_1 + I_2 + I_3 + I_4} = \frac{(2H + h) \tan \alpha_S}{d - e - h \operatorname{sgn} \alpha_S \tan \alpha_S} \quad (21)$$

$$R_\beta = \frac{(I_1 + I_2) - (I_3 + I_4)}{I_1 + I_2 + I_3 + I_4} = \frac{(2H + h) \tan \beta}{d - e - h \operatorname{sgn} \beta_S \tan \beta_S} \quad (22)$$

where $\operatorname{sgn}(\cdot)$ is the sign function.

Equations 21 and 22 can be inverted to compute the tangents of the angles of the sensors as a function of the measured centroids R_α and R_β :

$$\tan \alpha_S = \frac{(d - e) R_\alpha}{2H + h + h \operatorname{sgn}(R_\alpha) R_\alpha} \quad (23)$$

$$\tan \beta_S = \frac{(d - e) R_\beta}{2H + h + h \operatorname{sgn}(R_\beta) R_\beta} \quad (24)$$

250 where R_β and R_α are calculated from the measured intensities (equations 21 and 22).

Figure 6b shows the design of the sensor's printed circuit board (PCB). The quad-photodiode is a TT Electronics OPR5911 chip, placed at the center top of the board. The aperture was made from 0.002" (50 μm) thick black anodized
 255 aluminum foil (Thorlabs BKF12). The anodization prevents reflection inside the sensor. The aperture hole is 1.3 mm wide and was cut by a Universal Laser System XLS10 laser cutter using a 1.06 μm fiber laser. The sensing element weighs 0.2 g and the total mass of the sun sensor as built is 5 g.

Each photodiode is connected to a two-stage current-to-voltage amplifier
 260 (transimpedance and inverting amplifiers) to create a readable voltage at the pin of an Analog-to-Digital Converter (ATtiny84A). The ADC chip also handles the filtering of the data using an impulse response filter [33] and the communication to an external computer using the SPI protocol [34].

Two connectors on each side of the board allow multiple sensors to be con-
 265 nected in a daisy chain, sharing power and data lines. This scheme simplifies the connection of multiple sensors and reduces the electrical wiring.

All of the sensors were calibrated in the angle range $\pm 20^\circ$ before being placed on the structure. The calibration curves were used to correlate the sensor outputs to the measured angles. The uncertainty in the measured angles was estimated to be 0.5° (3σ).

4.2. Structure with Integrated Sensors

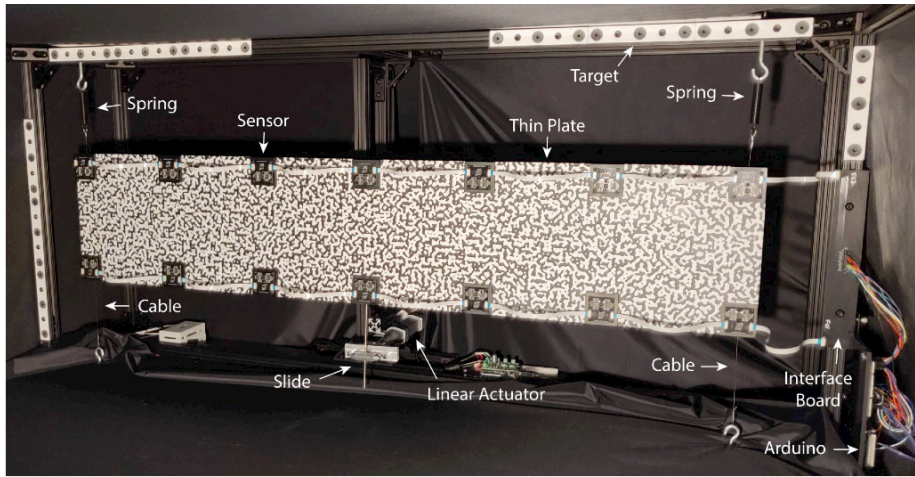


Figure 7: Photo of the experiment. A plate with a black and white Digital Image Correlation (DIC) pattern holds 14 sensors placed on rigid supports. The plate is held by tensioned spring cables at each end and two linear actuators in the middle (the actuator attached to the center of the structure is behind the plate).

The structure used for the experiment was a $0.016''$ (0.41 mm) thick, $50''$ (127 cm) long and $10''$ (25.4 cm) wide aluminum plate, figure 7. These dimensions were chosen such that the plate would fit on an optical table while also allowing the placement of multiple sensors.

Each PCB was attached on a $2'' \times 2''$ (50.8 mm \times 50.8 mm) stiff aluminum mount and held by four screws in order to avoid damage to the solder joints from the deformation of the aluminum plate. These mounts also prevent movement of the sensors during the experiment which would introduce errors in the measurements. The centers of the mounts were placed at a spacing of $8''$ (20.32 cm) in both directions, as seen in figure 7.

The structure was attached at both ends to steel cables mounted in series with a spring; a pre-tension of 35 N was applied. These supports effectively create simply supported boundary conditions for the structure.

285 The structure was deformed by means of two linear actuators placed in the middle (see figure 7). The top actuator was attached to the center of the plate, behind the structure in figure 7, using a pivot while the bottom actuator was connected through a pivot and a slide mechanism. When both actuators were actuated together, the structure underwent bending and when only the bottom
290 one was actuated, the structure underwent torsion.

Fourteen sensors were placed on the structure. They shared the same power and data lines in a daisy chain connection using Flat Flexible Cables (FFC) with a much lower bending stiffness than the aluminum sheet. An Arduino Due computer, mounted on a supporting structure, gathered the intensities of the 4
295 diodes, filtered using an impulse response filter, sent by each sensor, and relayed the measurements to a laptop via serial communication.

The light source used in the experiment was a white LED (SSR-90 from Luminus Devices Inc.). It generates about 1000 lumens which is matched with the gains of the sensors to generate a readable output. In order to avoid reflections
300 which could affect the reading of the sensors, the whole setup was covered in blackout fabric (BK5 from ThorLabs). A mask was placed in front of the LED to direct the light only towards the sensors, see figure 8.

In order to estimate the performance of the shape reconstruction method, an independent measurement system consisting of a Digital Image Correlation
305 (DIC) system from Correlated Solutions was used. It consisted of two cameras (Point Grey Grasshopper3, 5MP, Mono), pointed to the structure from a distance of 2 m (see figure 8). The Vic3D software was used to combine pairs of images taken simultaneously by the cameras to triangulate black and white markers on the structure. The accuracy of this system is on the order of 50
310 μm , i.e., about an order of magnitude better than the expected accuracy of the shape reconstruction algorithms.

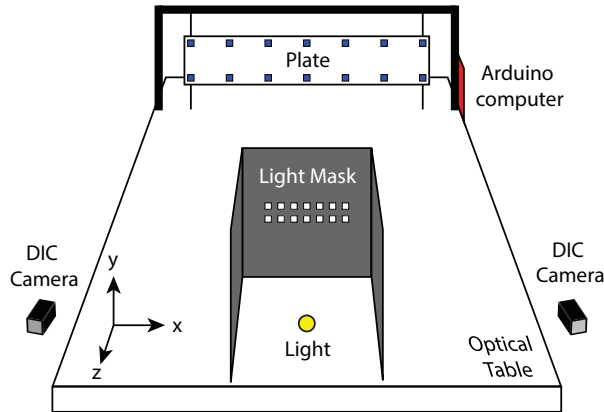


Figure 8: Schematic of test setup. The plate with 14 sensors is mounted at one end of an optical table with an Arduino computer retrieving the measurements, and the LED light is in an enclosed box at the other end. DIC cameras produce a reference measurement of the shape of the surface.

4.3. Algorithm Parameters

GISRA. Fifteen control points were used to define the reconstructed shape together with their respective Lagrange interpolating polynomials. The points
 315 were uniformly spaced on the 5×3 grid shown in figure 2. An inextensibility grid of 13×5 was used. Because the surface was located relatively far from the light source (about 2 m), the algorithm was not able to accurately estimate the distance, which would have led to large errors in the reconstruction. To remove this numerical singularity, the central point of the surface was fixed to its 3D
 320 position, obtained from the DIC measurements.

FESRA. Figure 9 shows the different load boundary conditions that were applied. They were used to generate the matrix \mathbf{F}_d using equation 15. A total of five loading conditions were considered, corresponding to the boundary conditions imposed on the test structure. In order to fix the shape to its local
 325 reference frame, the out-of-plane deflection of the nodes shown in blue in figure 9 was set equal to 0. Note that these constraints are associated with reaction forces that provide load boundary conditions and are explicitly calculated by

the model.

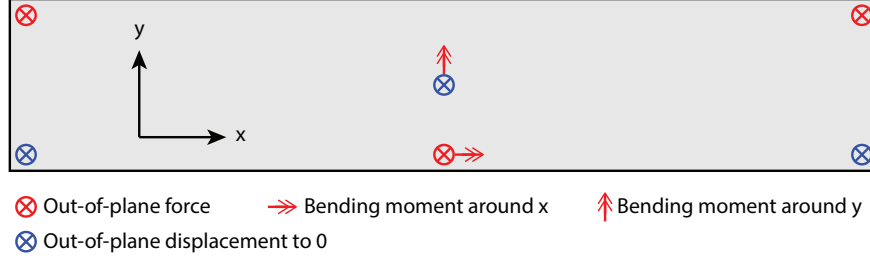


Figure 9: Boundary conditions of finite element model. The amplitude of each load is left as an unknown, determined from the angle measurements.

Similarly to GISRA, this algorithm has a numerical singularity which is associated with the distance from the surface to the light source. This issue was addressed by measuring the distance of the central point of the surface with the DIC system. The translation vector in equation 13 was then generated by introducing two rotation matrices:

$$\mathbf{t} = \mathbf{R}_x \mathbf{R}_y \mathbf{t}_0 \quad (25)$$

330 where \mathbf{t}_0 is the original position of the center of the structure, \mathbf{R}_x is the rotation matrix around the x -axis, and \mathbf{R}_y is the rotation matrix around the y -axis. The two angles defining the rotation matrices were used in the unknown vector (equation 16) instead of the 3 coordinates of the translation vector.

5. Experimental Results

335 Experiments were conducted on the structure presented in the previous section. Three sets of static deformations were imposed using the two actuators, including pure bending (see subsection 5.1), pure torsion (see subsection 5.2), and combinations of bending and torsion (see subsection 5.3).

340 The structure was deformed by moving the linear actuators and held in this shape. Then, pictures were taken by the DIC cameras under uniform light conditions. A total of 20 sets of images were taken to average out the DIC reconstruction and improve its accuracy. The experimental setup was then

covered with blackout fabric and the LED light was turned on. A total of 100 independent sets of measurements were taken with the sensors at a rate of 10 Hz, to obtain statistically significant results. The angles of each sensor were obtained using their respective calibration data. Each set of angle measurements was used to generate two reconstructed shapes, with GISRA and FESRA.

5.1. Bending Deformation

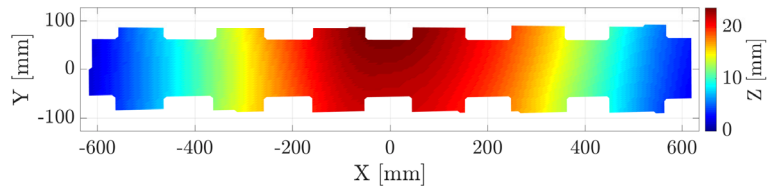
The structure was deflected at the center by imposing equal displacements with both actuators. Figure 10 shows the results of an experiment with a 20 mm deflection. The shape measured by DIC is shown in figure 10a. Note that DIC can only measure the central part of the structure as the cables connecting the sensors obstruct the view of the cameras. Figure 10b shows the mean shape reconstructed using GISRA, while figure 10c shows the shape obtained using FESRA. The mean shape was calculated by averaging the 100 reconstructed shapes from the 100 measurements.

The results are qualitatively similar as both sets capture the global deflection. A detailed map of the average error across the surface is shown in figure 11. FESRA does a slightly better job on the left of the structure and lower right, leading to a better accuracy (0.91 mm vs. 1 mm). The accuracy is mostly limited by errors on the right of the structure which may be due to inaccurate positioning of the sensors in this part of the plate.

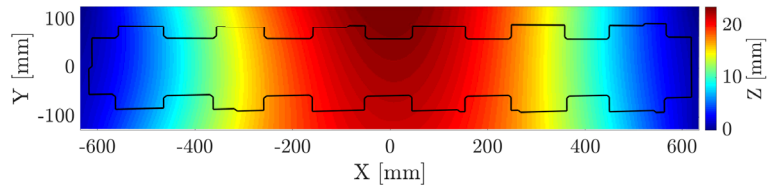
5.2. Torsional Deformation

Figure 12 shows the shape reconstruction for the structure undergoing torsion. The bottom actuator was moved 20 mm back while the middle actuator remained at its zero position, to impose a 5.2° rotation between the actuators. Because of the tension in the edge cables, the outer edges of the structure remained relatively straight while the center was twisted.

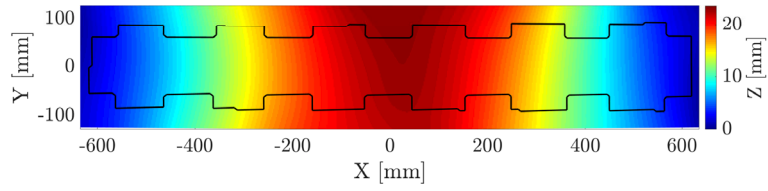
The results from the two algorithms are almost identical and show that they are both capable of reconstructing this more complex shape. The error, shown in figure 13, is close to zero, with some localized deformation around the center



(a) Shape measured by DIC system.



(b) Shape reconstructed by GISRA.



(c) Shape reconstructed by FESRA.

Figure 10: Measured and reconstructed shapes for 20 mm deflection at the center of the structure.

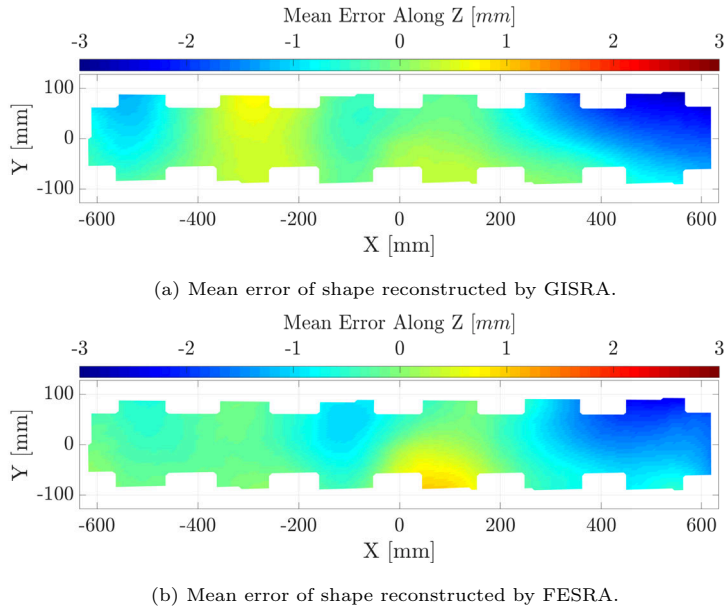


Figure 11: Error of reconstructed shapes for 20 mm deflection at the center of the structure.

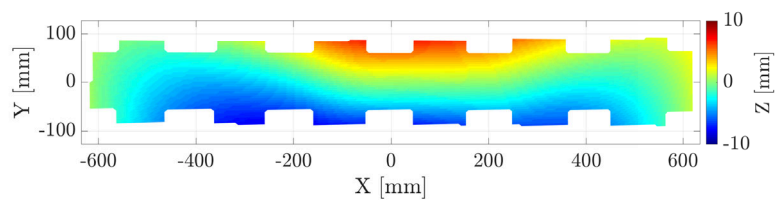
and the far right. While FESRA performs better on the left, GISRA is best on the right. Overall, both algorithms yielded an average RMS error of 0.55 mm.

5.3. Combination of Bending and Torsional Deformations

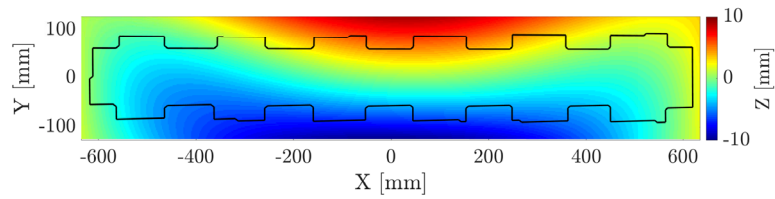
375 Both algorithms performed well for relatively small deformations of the structure, with average RMS errors under a millimeter. Differences arose when applying more complex (bending plus torsion), larger deformations to the structure.

Figure 14 shows the results after displacing the central actuator by -20 mm and the bottom one by -40 mm. While the overall shape is well captured, local features appear around the center of the structure which is reconstructed differently by the two algorithms. GISRA provides a relatively smooth reconstruction, see figure 14b, but cannot capture the inflection point shown by the turquoise outline. FESRA reconstructs this local deformation more accurately.

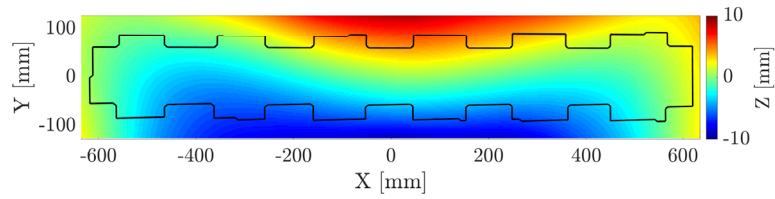
385 This is highlighted by the error plot in figure 15. While GISRA gives errors of almost 3 mm in amplitude around the center of the structure, FESRA does



(a) Shape measured by DIC system.



(b) Shape reconstructed by GISRA.



(c) Shape reconstructed by FESRA.

Figure 12: Measured and reconstructed shapes for 5.2° torsion at the center of the structure.

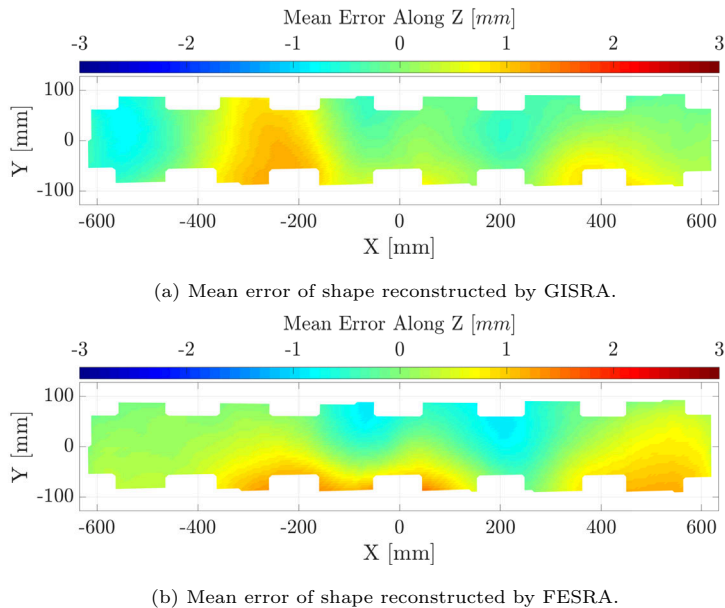
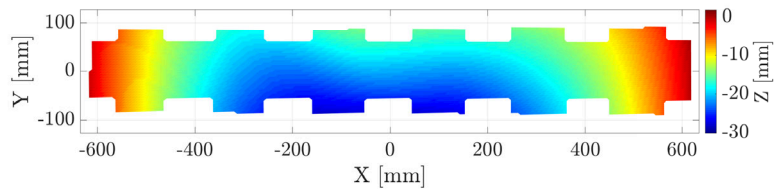


Figure 13: Error of reconstructed shapes for 5.2° torsion at the center of the structure.

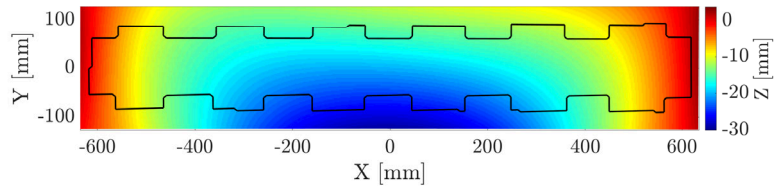
not produce such a distinctive pattern, especially on the right. This leads to an RMS error of 0.97 mm, 20% better than GISRA (1.21 mm).

Additional measurements were carried out for a range of deformations, combining different amounts of bending and torsion of the structure. The results are presented in figure 16, showing the average RMS error for all shapes considered. These deformations span a range of deflection from -20 mm to 20 mm and torsion from -5.2° to 5.2° . The error for smaller deformations is low and comparable for both algorithms. As the amplitude of the applied displacement increases, more local features appear which increases the complexity of the deformation field. GISRA loses accuracy for such shapes, due to the relatively sparse representation of the deformation caused by the limited number of control points. FESRA, on the other hand, remains accurate and is less sensitive to the amplitude and complexity of the deformation.

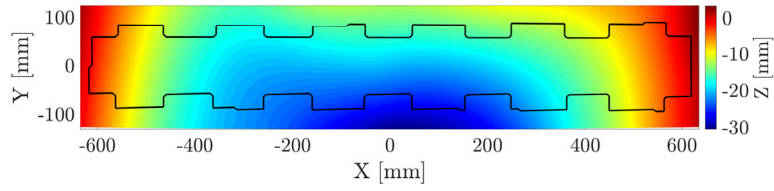
Overall, figure 16 shows that FESRA provides much better results than GISRA with approximately a factor 1.5 increase in accuracy overall. The aver-



(a) Shape measured by DIC system.



(b) Shape reconstructed by GISRA.



(c) Shape reconstructed by FESRA.

Figure 14: Measured and reconstructed shapes for -20 mm deflection and 5.2° torsion of the structure.

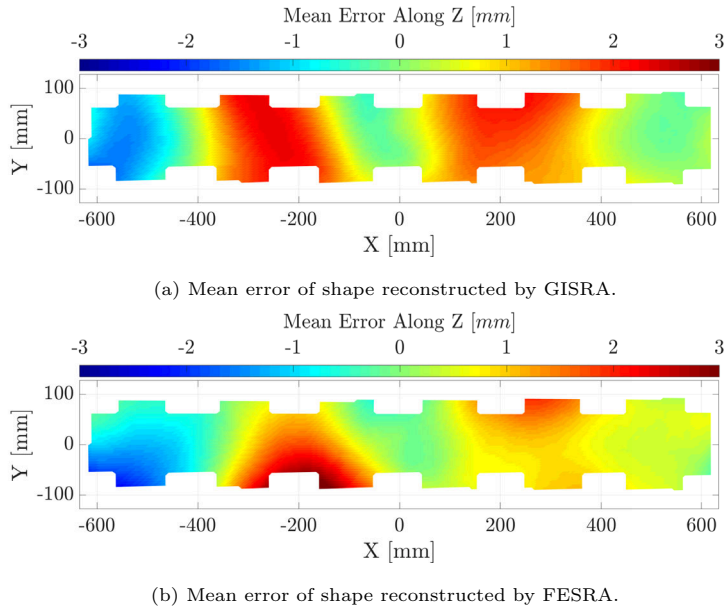


Figure 15: Error of reconstructed shapes for -20 mm deflection and 5.2° torsion of the structure.

age RMS error for GISRA over the different experiments represented in figure 16 is 1.25 mm and decreases to 0.9 mm with FESRA. The accuracy improvements are as high as 70% for some specific combinations of deflection and torsion.

405 5.4. Computational Time

It took about 150 ms to calculate the position of the control points (45 unknowns) with GISRA on an Intel Core i5-6200U CPU, and about 30 s to estimate the full set of unknowns (1690) with FESRA. This large difference in computational times is mostly due to the much larger number of unknowns and the use of a finite difference scheme to compute most of the Jacobian matrices. However, it should also be noted that no attempt was made to optimize the speed of the algorithms in this research, and the FESRA method could be significantly sped up through the use of standard model reduction techniques.

415 Additionally, faster methods than the Levenberg-Marquardt solver and the explicit calculation of the Jacobian matrix or linearization of the constraints are some of the possible ways to increase the speed of the presented shape

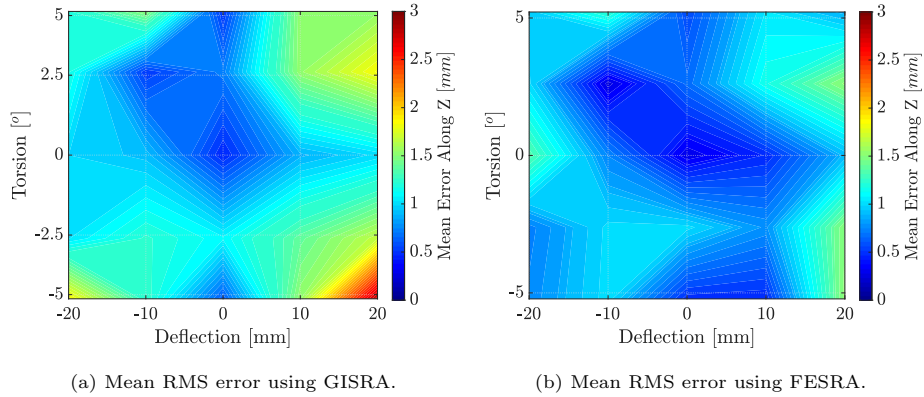


Figure 16: Mean RMS error of the reconstructed shape for a range of applied deflections and torsions.

reconstruction algorithms.

6. Conclusion and Discussion

This paper has presented and demonstrated two approaches to reconstruct
 420 the shape of a planar structure using distributed sun angle measurements. The
 algorithms were tested on a 1.3 m \times 0.25 m aluminum thin plate with 14
 embedded sensors, deformed at the center by a few centimeters in a combination
 of bending and torsion modes.

The geometric, inextensible shape reconstruction algorithm (GISRA) uses
 425 the sensor measurements together with the assumption that the mid-plane of
 the structure does not stretch. Millimeter level accuracy is achievable, as measured
 in the experiments. The method is limited by the complexity of the shape
 induced by local deformations; only smooth surfaces can be reconstructed accurately.

430 To improve the accuracy of the algorithm, a mechanical model of the structure
 was introduced to predict local deformations. The stiffness equations replaced
 the inextensibility conditions of GISRA, and a net improvement of accuracy
 by over 40% was shown together with an improved sensitivity to local

deformations. FESRA is however much slower in the present implementation,
435 which would limit its use for time sensitive applications such as real-time shape
reconstruction, although it was noted in section 5.4 that model reduction tech-
niques could be used to speed up the FESRA method.

More work still remains to implement these algorithms in flight systems. The
finite element model of FESRA is limited to small deformations and for some
440 applications it may need to be made more general to include a geometrically
nonlinear finite element model instead. This would add complexity to the system
of equations and make the algorithm slower, but also suited to a wider range of
applications.

Also, the performance of both algorithms should be tested for more complex
445 geometries and larger deflections to better understand the limits and range of
applicability.

Only static shapes were considered for this research and more work could
be undertaken to apply each algorithm to dynamic structural response. Filter-
ing techniques such as Kalman filters could be introduced using the equations
450 presented in this paper to improve the accuracy of the solution.

It should be noted that the system of equations in both algorithms can be
linearized if small deformations are expected and if the incident light on the
structure is collimated (which is a good approximation for sunlight). Lineariza-
tion would greatly accelerate the solution process which could be advantageous
455 for applications where computational resources are limited.

Turning to the practical implementation of the proposed system, an obvious
next step is the miniaturization of the sun sensor into an integrated circuit.
Also, depending on the specific application, the field of view of the sun sensor
presented in this paper may be deemed too small. Sensors at different angles
460 could be placed in a row to cover a wider range of angles, or the present design
could be modified to an extended angle range. The effects of light reflected from
other planets should also be considered. A possible approach would be to con-
sider either the overall effect on system error or, depending on the application,
measurements polluted by a spurious light source could be discarded.

465 **Acknowledgments**

Suggestions from the Space Solar Power Project team at Caltech are acknowledged. This research was supported by the Space Solar Power Project at Caltech.

References

- 470 [1] M. Berger, A. Tagliasacchi, L. M. Seversky, P. Alliez, G. Guennebaud, J. A. Levine, A. Sharf, C. T. Silva, A Survey of Surface Reconstruction from Point Clouds, in: *Computer Graphics Forum*, Vol. 36, Wiley Online Library, 2017, pp. 301–329.
- [2] A. Khatamian, H. R. Arabnia, Survey on 3D Surface Reconstruction, *Journal of Information Processing Systems* 12 (3).
475
- [3] F. Brunet, R. Hartley, A. Bartoli, N. Navab, R. Malgouyres, Monocular Template-Based Reconstruction of Smooth and Inextensible Surfaces, in: *Asian Conference on Computer Vision*, Springer, 2010, pp. 52–66.
- [4] M. Perriollat, R. Hartley, A. Bartoli, Monocular Template-Based Reconstruction of Inextensible Surfaces, *International Journal of Computer Vision* 95 (2) (2011) 124–137.
480
- [5] M. Salzmann, J. Pilet, S. Ilic, P. Fua, Surface Deformation Models for Nonrigid 3D Shape Recovery, *IEEE Transactions on Pattern Analysis and Machine Intelligence* 29 (8) (2007) 1481–1487.
- 485 [6] F. Brunet, A. Bartoli, R. I. Hartley, Monocular Template-Based 3D Surface Reconstruction: Convex Inextensible and Nonconvex Isometric Methods, *Computer Vision and Image Understanding* 125 (2014) 138–154.
- [7] A. Bartoli, Y. Gérard, F. Chadebecq, T. Collins, D. Pizarro, Shape-From-Template, *IEEE Transactions on Pattern Analysis and Machine Intelligence* 37 (10) (2015) 2099–2118.
490

- [8] A. Chhatkuli, D. Pizarro, A. Bartoli, T. Collins, A Stable Analytical Framework for Isometric Shape-From-Template by Surface Integration, *IEEE Transactions on Pattern Analysis and Machine Intelligence* 39 (5) (2016) 833–850.
- 495 [9] M. Gallardo, T. Collins, A. Bartoli, Dense Non-Rigid Structure-From-Motion and Shading with Unknown Albedos, in: *Proceedings of the IEEE International Conference on Computer Vision*, 2017, pp. 3884–3892.
- [10] A. Varol, A. Shaji, M. Salzmann, P. Fua, Monocular 3D Reconstruction of Locally Textured Surfaces, *IEEE Transactions on Pattern Analysis and Machine Intelligence* 34 (6) (2012) 1118–1130.
- 500 [11] A. W. Burner, W. A. Lokos, D. A. Barrows, In-flight Aeroelastic Measurement Technique Development, in: *Optical Diagnostics for Fluids, Solids, and Combustion II*, Vol. 5191, International Society for Optics and Photonics, 2003, pp. 186–199.
- 505 [12] A. Lizotte, W. Lokos, Deflection-Based Aircraft Structural Loads Estimation with Comparison to Flight, in: *46th AIAA/ASME/ASCE/AHS/ASC Structures, Structural Dynamics and Materials Conference*, 2005, p. 2016.
- [13] A. Hermanis, R. Cacurs, M. Greitans, Acceleration and Magnetic Sensor Network for Shape Sensing, *IEEE Sensors Journal* 16 (5) (2015) 1271–1280.
- 510 [14] M. Huard, N. Sprynski, N. Szafran, L. Biard, Reconstruction of Quasi-Developable Surfaces From Ribbon Curves, *Numerical Algorithms* 63 (3) (2013) 483–506.
- [15] N. Sprynski, B. Lacolle, L. Biard, Motion Capture of an Animated Surface via Sensors’ Ribbons, in: *PECCS 2011-1st International Conference on Pervasive and Embedded Computing and Communication Systems*, SciTePress, 2011, pp. 421–426.
- 515

- [16] T. Hoshi, H. Shinoda, 3D Shape Measuring Sheet Utilizing Gravitational and Geomagnetic Fields, in: 2008 SICE Annual Conference, IEEE, 2008, pp. 915–920.
- 520 [17] T. Stanko, S. Hahmann, G.-P. Bonneau, N. Saguin-Sprynski, Shape From Sensors: Curve Networks on Surfaces From 3D Orientations, *Computers & Graphics* 66 (2017) 74–84.
- [18] R. C. Boden, J. Hernando-Ayuso, Shape Estimation of Gossamer Structures Using Distributed Sun-Angle Measurements, *Journal of Spacecraft and Rockets* 55 (2) (2017) 415–426.
- 525 [19] T. Talon, S. Pellegrino, In-Space Shape Measurement of Large Planar Structures, in: 4th AIAA Spacecraft Structures Conference, 2017, p. 1116.
- [20] T. Talon, S. Pellegrino, Shape Measurement of Large Structures in Space: Experiments, in: 2018 5th IEEE International Workshop on Metrology for AeroSpace (MetroAeroSpace), IEEE, 2018, pp. 581–584.
- 530 [21] L. Salgado-Conrado, A Review on Sun Position Sensors Used in Solar Applications, *Renewable and Sustainable Energy Reviews* 82 (2018) 2128–2146.
- [22] M. A. Post, J. Li, R. Lee, A Low-Cost Photodiode Sun Sensor for CubeSat and Planetary Microover, *International Journal of Aerospace Engineering* 2013.
- 535 [23] F. J. Delgado, J. M. Quero, J. Garcia, C. L. Tarrida, P. R. Ortega, S. Bermejo, Accurate and Wide-Field-of-View MEMS-Based Sun Sensor for Industrial Applications, *IEEE Transactions on Industrial Electronics* 59 (12) (2012) 4871–4880.
- 540 [24] G. Wang, F. Xing, M. Wei, Z. You, Precision Enhancement Method for Multiplexing Image Detector-Based Sun Sensor With Varying and Coded Apertures, *Applied Optics* 54 (35) (2015) 10467–10472.

- [25] L. Farian, P. Häfliger, J. A. Leñero-Bardallo, A Miniaturized Two-Axis Ultra Low Latency and Low-Power Sun Sensor for Attitude Determination of Micro Space Probes, *IEEE Transactions on Circuits and Systems I: Regular Papers* 65 (5) (2017) 1543–1554.
- [26] F. Chen, J. Feng, Analogue Sun Sensor Based on the Optical Nonlinear Compensation Measuring Principle, *Measurement Science and Technology* 18 (7) (2007) 2111.
- [27] Z. Peterson, Second Generation Wallops Fine Sun Sensor, in: 29th Annual AIAA/USU Conference on Small Satellite, AIAA, 2016.
- [28] T. Talon, Surface Reconstruction from Distributed Angle Measurements, PhD Dissertation, Caltech (2020).
- [29] E. Kreyszig, Introduction to Differential Geometry and Riemannian Geometry, University of Toronto Press, 1968.
- [30] E. Abbena, S. Salamon, A. Gray, Modern Differential Geometry of Curves and Surfaces with Mathematica, Chapman and Hall/CRC, 2017.
- [31] R. D. Cook, D.S. Malkus, M.E. Plesha, R.J. Witt, Concepts and Applications of Finite Element Analysis, Fourth Edition, John Wiley & Sons, 2002.
- [32] J.-L. Batoz, K.-J. Bathe, L.-W. Ho, A Study of Three-Node Triangular Plate Bending Elements, *International Journal for Numerical Methods in Engineering* 15 (12) (1980) 1771–1812.
- [33] P. Regalia, Adaptive IIR Filtering in Signal Processing and Control, Routledge, 2018.
- [34] F. Leens, An Introduction to I²C and SPI Protocols, *IEEE Instrumentation & Measurement Magazine* 12 (1) (2009) 8–13.